ARCHIVE OF MECHANICAL ENGINEERING

DOI: 10.24425/ame.2022.155869 2025, Vol. 72, No. 3, pp. 405–433

Ivana LINKEOVÁ [1], Tomáš BODNÁR [1,2], Anna LANCMANOVÁ [1,2,3], Luboš PIRKL [3]

New parametric computational test case for automated design and analysis of an axial blood pump

Received 30 June 2025, **Revised** 25 August 2025, **Accepted** 17 September 2025, **Published online** 21 September 2025

Keywords: parametric geometrical model, automated design, ventricular assist device, axial blood pump, incompressible Navier-Stokes equations, OpenFOAM

The paper presents a new fully parametric geometrical model of a ventricular assist device (VAD) together with an example of a comprehensive automated workflow integrating multidisciplinary tools for geometrical design, fluid dynamic assessment, and automated shape optimisation. Advanced geometrical constructions are applied to develop a new fully parametric CAD (Computer Aided Design) model that generates a stable, watertight geometry of an axial blood pump in both non-uniform B-spline representation and node-to-node triangular mesh.

The presented example of a fully integrated simulation workflow that combines open-source software tools within a user-friendly environment, demonstrates its efficiency while benefiting from the fully parametric, easily adjustable VAD model. The proposed geometrical modelling and numerical simulation approach offers a seamless, ready-to-use test case for computer aided design, analysis and optimisation of VADs. The shown results demonstrate the essential advantages of the parametric modelling approach, showcasing its potential application in performance improvements of an axial blood pump through shape optimisation. Overall, the paper highlights the viability of automated, multidisciplinary design workflows in biomedical engineering.

✉ Ivana LINKEOVÁ, email: ivana.linkeova@fs.cvut.cz

[1]Czech Technical University in Prague, Faculty of Mechanical Engineering, Prague, Czech Republic

[2]Czech Academy of Sciences, Institute of Mathematics, Prague, Czech Republic

[3]CFD support, s.r.o., Prague, Czech Republic

Emails: tomas.bodnar@fs.cvut.cz, anna.lancmanova@fs.cvut.cz, lubos.pirkl@cfdsupport.com

1. Introduction

This paper presents the construction and example of application of a new computational test case. It is motivated by the design of mechanical aids of human cardiovascular system, namely the Ventricular Assist Devices (VADs). These are small auxiliary blood pumps that augment the blood flow in the circulatory system by helping the weak and failing hearth to provide sufficient blood flow and pressure in the human body. These mechanical rotary blood pumps are high-performance devices that need to be carefully designed to provide high performance and efficiency while preserving small size and low power consumption [1, 2]. Further design constrains arise from the need for bio-compatibility of the device, namely from the risks of hemolysis (the mechanical damage of red blood cells) and thrombus formation [3, 4].

The experimental investigation of such devices is very complicated and expensive, despite the fact that in most cases it can only provide global parameters of the device, without revealing the complete details of the structure of the local blood flow field [5]. This is why the use of Computational Fluid Dynamics (CFD) is one of the key instruments in the analysis and design of VADs. Even with the use of CFD simulations (sometimes called in-silico models) the development and optimisation of blood pumps is very expensive and time-consuming. There exist large number of CFD simulations and studies focusing on various particular aspects of the VADs design and their numerical assessment. The essential flow features are discussed, for example, in [1],[6],[7, 8], the turbulence effects in [4],[2],[5], the non-Newtonian rheology was used in [9],[10]. The hemolysis (blood damage caused by mechanical stress) is of primary interest in [11],[12],[3]. These numerous studies were performed for different VADs, ranging from simple academic designs up to quite realistic shapes similar to those being commercially produced and implanted to patients.

One of the key obstacles in faster progress in modelling of flow and other biomedical processes in blood pumps is in the rather complicated geometry of the device and the wide variety of different designs used by different researchers and producers. This makes the individual studies performed on different geometries difficult to compare and to assess the mutual performance of various mathematical models of blood rheology, hemolysis, and thrombosis. In addition, majority of the used VAD geometries are not fully disclosed, so it is virtually impossible to replicate the published simulations or use the identical geometry for further studies by other researchers.

A lack of a simple, but yet realistic common geometrical model of VAD, which can be used by different authors, led us to the development of a new geometrical design of a generic VAD that can be used for this purpose. In order to be able to assess also the influence of different geometrical parameters on the blood pump performance, efficiency and bio-compatibility, the model was created as fully parametric, being completely defined by a list of geometrical parameters that can be

varied if needed. This kind of fully parametric design is not only suitable for performing case studies looking into the effect of individual model parameters, but is also perfectly suited for automated shape optimisation, possibly leading to new designs of advanced VADs.

Geometry variability proves to be a key factor in optimising the performance of blood pumps, as its systematic changes allow analysing the influence of design parameters on the hydraulic performance and hemodynamic compatibility of the VAD [6, 13]. In [6], the design of the impeller and diffuser blades of the left VAD was systematically modified using a few selected geometrical parameters to obtain different variants. Then, the effect of these geometrical variables on the hydraulic performance of the pump was analysed using statistical models. In [13], selected geometrical parameters were systematically varied and their effects on the hemodynamics and hydraulic performance of a centrifugal blood pump designed according to industry guidelines were investigated using CFD.

The main aim of this paper is to present a new computational test case of an axial blood pump, including an example of the complete automated workflow.

It starts by the generation of a fully parametric Computer Aided Design (CAD) model, followed by its computational evaluation by means of CFD simulations, postprocessing of the resulting data, their assessment and final report generation.

The showcased workflow integrates a fully parametric geometry generation into the CFD simulation loop based on the automated shape optimisation process. This advanced concept makes it possible to further improve the VAD design, helping to reduce numerous medical complications, allowing to downsize the device, or enabling its better regulation to allow for active patient lifestyle [14].

The structure of the paper is as follows: The Introduction is followed by a detailed description of the geometrical construction and generation of the CAD model in Section 2. The model surface mesh generation and export is briefly explained in Section 3. The example of use of the newly developed VAD model within an advanced simulation workflow is shown in the remaining part of the paper. The basics of the computational grid generation, numerical flow simulations, their automated evaluation and reporting are given in Section 4. Finally, an introduction to the automated process of shape optimisation is shown in Section 5.

This paper follows the short proceedings contribution [15], where the first version of a newly developed parametric CAD model of a VAD was briefly introduced and preliminary CFD simulations were presented. Here, the process of generation of an axial blood pump parametric CAD model is described in detail, including the incorporation of the generated 3D geometry into CFD simulations.

2. Geometrical construction of a model of an axial blood pump

The basic concept (architecture) and dimensional parameters of the proposed new simplified VAD model were chosen as a compromise based on previous published works of different authors. The most important inspirations include [16]

focused on the design and development of an axial left VAD for adults, [7, 8], where the design of an axial blood pump and its improved version based on the application of CFD techniques are presented, [17] with the design of an axial blood pump with a rotor on magnetic bearings and [2], where the design of a VAD intended for research purposes was inspired by clinical devices with axial flow.

The considered shape represents a simplified working model of a generic axial VAD, that retains most of the common flow characteristics and design features found in real VADs being currently in medical use. This simplification allows for representing the whole geometry by a limited set of parameters, defining a fully adjustable model geometry to be used for research and development purposes.

2.1. Tools and methods

The fully automated script-based process for generating the parametric geometry of the blood pump, its use in CFD simulations, and assessment of its performance characteristics is shown schematically in Fig. 1.

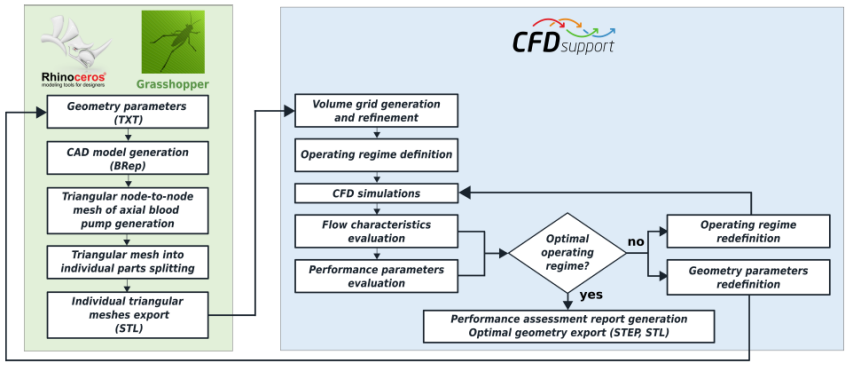

Fig. 1. Schematics of the automated process of 3D geometry generation, CFD simulation and shape optimisation

To develop a fully parametric geometrical model of an axial blood pump, 3D computer graphics and CAD software Rhinoceros with an integrated Grasshopper graphical algorithm editor was chosen. The choice of this software environment was influenced by the fact that Rhinoceros not only excels in modelling spatial objects using mathematically precise Non-Uniform B-Spline (NURBS) representation [18], but also provides advanced support for polygon meshes. Therefore, the generated geometry can be exported in NURBS representation as smooth surfaces (e.g., STEP, IGES, SAT format) or as a triangular node-to-node mesh in STL format. This desirable feature of the chosen modelling software and the adopted model mathematical representation is the key aspect for automatically generating high quality scalable geometries and computational grids without compromising the smoothness of the model surfaces and their perfect watertight fit for the whole range of admissible parameters.

The most common type of modelling in CAD applications, the so called boundary representation (BRep), is used to develop the blood pump CAD model. BRep is a mathematically precise virtual representation where the modelled object is defined by the boundaries of its volume [19]. A solid in BRep is represented by a closed watertight polysurface, as a result of which a triangular node-to-node mesh can be generated.

The process of the CAD model generation is based on the set of shape parameters listed in Tab. 1 with respect to the coordinate system given in Fig. 2. Once the text file with shape parameters is updated, the generation of a new geometry starts and all constructions described below are carried out automatically in Grasshopper with a software tolerance of 0.001 mm. No additional manual interventions are required during and after the geometry generation.

The design of the entire geometry shown in Fig. 2 is subject to the computational requirements. Individual surfaces of the CAD model include both physical boundaries and fictitious interfaces between the future modelling sub-domains and computational grid blocks. For numerical simulations, the whole solution domain is bounded by a long straight shroud, inside of which the actual blood pump is placed for numerical testing. The artificial inlet and outlet boundaries are placed far enough to allow the flow to fully develop and settle.

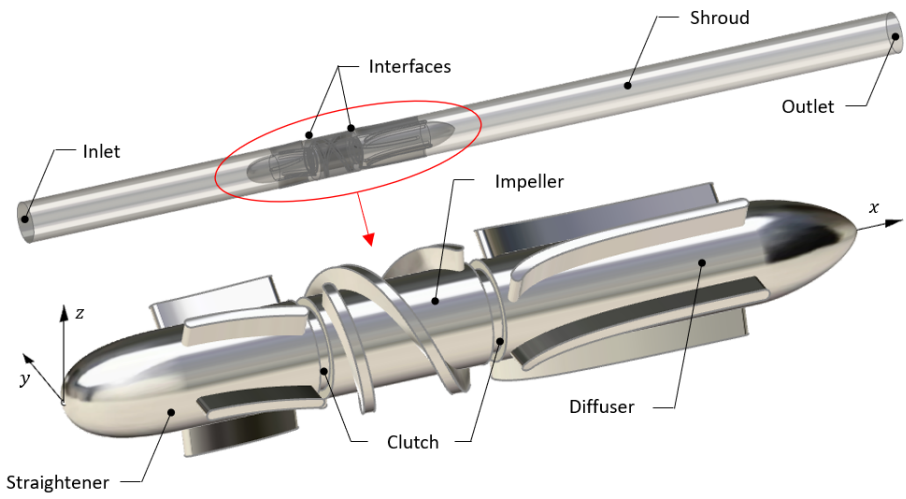

Fig. 2. Structure of the CAD model of an axial blood pump

In the procedure of the CAD model development, a number of common modelling techniques and geometrical transformations are applied to generate curves used to create surfaces with the required geometrical properties [20, 21]. Since the n-th-degree Bézier curve $\mathbf{C}(u)$, $u \in [0, 1]$, is used as the generating curve of many surfaces in the presented CAD model of the blood pump, its vector equation is given here.

Table 1. Set of input parameters for data export and geometry generation

Symbol	Parameter	Dimension
Folder	Path to the existing folder for STL export	
D	Shroud diameter	16 mm
DT	Tip diameter	15.76 mm
DH	Hub diameter	11 mm
DC	Clutch diameter	11 mm
L	Shroud length	380 mm
LSS	Stator shroud length	127 mm
LS	Straightener length	27 mm
LSF	Straightener front length	12 mm
LI	Impeller length	18.3 mm
LD	Diffuser length	40 mm
LC	Clutch length	0.7 mm
n_S	Straightener blades number	5
n_I	Impeller blades number	2
n_D	Diffuser blades number	3
TSB	Straightener blades thickness	1.2 mm
TIB	Impeller blades thickness	1.2 mm
TDB	Diffuser blades thickness	1.25 mm
LDB	Diffuser blades length	28 mm
WDB	Diffuser blades width	4 mm
s	Blades offset	0.75 mm
w	Helix wrap angle	360°
p	Helix shape parameter	1.75
a_1	Straightener meridian definition	3.5 mm
a_2	Straightener meridian definition	8.5 mm
b_1	Diffuser meridian definition	7.5 mm
b_2	Diffuser meridian definition	0 mm
b_3	Diffuser meridian definition	3 mm
c_1	Diffuser blade centre line definition	3 mm
c_2	Diffuser blade centre line definition	6 mm
d_1	Straightener blade centre line definition	-1.5 mm

$$\mathbf{C}(u) = \sum_{i=0}^{n} B_{i,n}(u)\mathbf{V}_i, \tag{1}$$

where $\mathbf{V}_i = (x_i, y_i, z_i)$, $i = 0, \ldots, n$, are control points and basis functions

$$B_{i,n}(u) = \binom{n}{k} u^i (1-u)^{n-i}, \ u \in [0,1], \ i = 0, \ldots, n, \tag{2}$$

are n-th-degree Bernstein polynomials.

Throughout of this section, the following convention is used to denote geometrical figures: $\mathbf{X}(u)$ denotes the mathematical model of the figure, $\mathbf{X}$ its CAD representation.

The CAD model of the blood pump, shown in Fig. 2, consists of three essential parts – *straightener*, *impeller* and *diffuser* separated by two clutches. The following subsections describe the detailed procedure for constructing their geometry. The individual subsections are presented in the same order in which the construction is programmed in Grasshopper, which helps to clarify the mutual relationships of the individual shape parameters in the entire parametric CAD model.

2.2. Straightener modelling

The hub of the straightener consists of two surfaces of revolution – front part $\mathbf{S}_{\mathrm{SF}}$ and cylindrical part $\mathbf{S}_{\mathrm{SH}}$. Surface $\mathbf{S}_{\mathrm{SF}}$ is generated by revolution of meridian $\mathbf{M}_{\mathrm{SF}}$ around the blood pump axis, which is identical with x-axis. Meridian $\mathbf{M}_{\mathrm{SF}}$ is 3rd-degree Bézier curve given by control points

$$\mathbf{V}_0 = (0,0,0), \mathbf{V}_1 = (0,0,a_1), \mathbf{V}_2 = (LSF - a_2, 0, rH), \mathbf{V}_3 = (LSF, 0, rH), \quad (3)$$

where $rH = DH/2$ is the hub radius. To ensure appropriate shape variability of the straightener hub, parameters a_1 and a_2 are limited to $a_1 \in (0, DH/2]$ and $a_2 \in (0, LSF)$.

Points

$$\mathbf{V}_3, \mathbf{V}_4 = (LS, 0, rH), \mathbf{V}_5 = (LS, 0, rH - rC), \quad (4)$$

where $rC = DC/2$ is the clutch radius, are vertices of piecewise linear meridian $\mathbf{M}_{\mathrm{SH}}$, the definition curve of surface $\mathbf{S}_{\mathrm{SH}}$, see Fig. 3a.

Configuration (3) of control points ensures that meridian $\mathbf{M}_{\mathrm{SF}}$ always has a tangent parallel to z-axis at point $\mathbf{V}_0$ and parallel to x-axis at point $\mathbf{V}_3$. Thus, the tangent continuity of surfaces $\mathbf{S}_{\mathrm{SF}}$ and $\mathbf{S}_{\mathrm{SH}}$ along the boundaries in plane $x = LSF$ is preserved, see Fig. 3b, even if the corresponding input shape parameters listed in Table 1 are changed.

For straightener blade modelling, its mean camber line $\mathbf{C}_{\mathrm{S}}$ as 2nd-degree Bézier curve in plane (x, z) given by control points

$$\mathbf{V}_6 = (x_3 + s + \tfrac{TSB}{2}, 0, 0), \mathbf{V}_7 = (x_6 + \tfrac{LSB}{2}, 0), \mathbf{V}_8 = (x_6 + LSB, 0, d_1) \quad (5)$$

is modelled first, see Fig. 3c. The orientation of the straightener blade is controlled by the sign of parameter d_1: for $d_1 < 0$ the blade bends clockwise, the blade is straight for $d_1 = 0$, and for $d_1 > 0$ the blade bends counter-clockwise with respect to (x, z) plane. For the next construction, mean camber line $\mathbf{C}_{\mathrm{S}}$ is extruded in negative y-direction by vector $(0, -r - 2, 0)$ to create auxiliary surface $\mathbf{E}_{\mathrm{S}}$, see Fig. 3d. The shroud radius $r = D/2$. Extending the extrusion by 2 mm is sufficient to ensure the existence of intersections in the following steps.

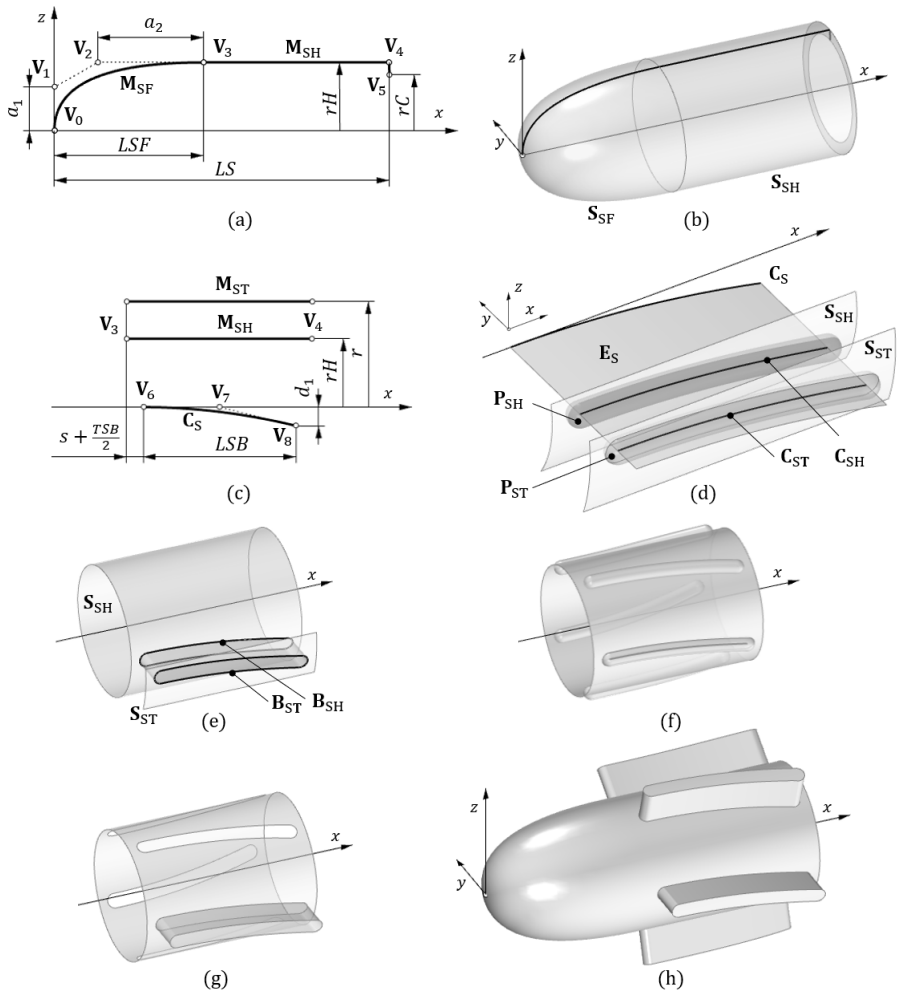

Fig. 3. Straightener modelling

Then, a part of auxiliary cylindrical surface $\mathbf{S}_{ST}$ with meridian $\mathbf{M}_{ST} \parallel \mathbf{M}_{SH}$ is created, see Fig. 3c and d. The cylindrical surface $\mathbf{S}_{ST}$ defines the tip of the straightener blade. Meridian $\mathbf{M}_{ST}$ is obtained by shifting the meridian $\mathbf{M}_{SH}$ by vector $(0, 0, r - rH)$, i.e., there is no gap between the shroud and the straightener blades. Mean camber lines $\mathbf{C}_{SH} = \mathbf{E}_S \cap \mathbf{S}_{SH}$ and $\mathbf{C}_{ST} = \mathbf{E}_S \cap \mathbf{S}_{ST}$ are constructed as intersections of surface $\mathbf{E}_S$ and the corresponding cylindrical surfaces.

In the next step, two pipes $\mathbf{P}_{SH}$ and $\mathbf{P}_{ST}$ of the same radius $TSB/2$ and rounded ends are constructed. The directing curves of the pipes are mean cumber lines $\mathbf{C}_{SH}$ and $\mathbf{C}_{ST}$, see Fig. 3d. Intersections $\mathbf{B}_{SH} = \mathbf{S}_{SH} \cap \mathbf{P}_{SH}$ and $\mathbf{B}_{ST} = \mathbf{S}_{ST} \cap \mathbf{P}_{ST}$ of the pipes with hub and tip cylindrical surfaces define the boundary curves of the straightener blade, see Fig. 3e. Pipe $\mathbf{P}_{SH}$ is n_S times copied around x-axis, see

Fig. 3f, to obtain cutting objects to create holes shaped according to curve $\mathbf{B}_{SH}$ in the straightener hub, see Fig. 3g.

The straightener blade is a composition of the ruler surface given by boundary curves $\mathbf{B}_{SH}$ and $\mathbf{B}_{ST}$ and the tip surface given by the inner part of cylindrical surface $\mathbf{S}_{ST}$ after cutting by the pipe $\mathbf{P}_{ST}$, see Fig. 3g. Finally, the straightener blade is copied n_S times around x-axis and the BRep of the straightener is finished, see Fig. 3h.

Using pipes with rounded ends to define boundary curves $\mathbf{B}_{SH}$ and $\mathbf{B}_{ST}$ results in curves $\mathbf{B}_{SH}$ and $\mathbf{B}_{ST}$ being offset curves to the mean cumber lines $\mathbf{C}_{SH}$ and $\mathbf{C}_{ST}$, i.e., the straightener blades have constant thickness TSB and rounded ends.

2.3. Impeller modelling

The impeller construction, following the straightener construction, is derived from the position of point $\mathbf{V}_5$ given by (4). The basic shape of the impeller hub is the surface of revolution $\mathbf{S}_{IH}$ with piecewise linear meridian $\mathbf{M}_{IH}$ given by vertices

$$\begin{aligned} \mathbf{V}_9 &= (x_5 + LC, 0, rC), \mathbf{V}_{10} = (x_9, 0, rH), \\ \mathbf{V}_{11} &= (x_9 + LI, 0, rH), \mathbf{V}_{12} = (x_{11}, 0, rC). \end{aligned} \tag{6}$$

To define the tip surface of the impeller blades, the auxiliary surface of revolution $\mathbf{S}_{IT}$ with meridian $\mathbf{M}_{IT}$ is constructed, see Fig. 4a and b. Meridian $\mathbf{M}_{IT}$ is obtained by shifting the line segment $\mathbf{V}_{10}\mathbf{V}_{11}$ of meridian $\mathbf{M}_{IH}$ by vector $(0, 0, rT - rH)$, where $rT = DT/2$ is the tip radius of the impeller blades. The difference $r - rT$ determines the radial gap between the shroud and the impeller blades. The radial gap is an important component of the blood pump, and its size can significantly influence the hemodynamic properties of the pump, especially at low flow rates [12].

Impeller blade is a right-hand oriented helicoidal surface generated by screw motion of a rectangular profile perpendicular to both the directing helix and axis of screw motion (x-axis). The principle of impeller operation requires a variable cross-section area between the blades. The screw motion is therefore a combination of translation along x-axis and rotation around x-axis, with the distance of translation not being directly proportional to the angle of rotation. Thus, the generating helix $\mathbf{H}(v)$ is given by

$$\mathbf{H}(v) = \left(\frac{h v^p}{w^p}, rH\cos(v), rH\sin(v) \right), v \in [0, w], \tag{7}$$

where $h = LI - 2s - TIB$ is the height of the helix. Helix shape parameter p controls the disproportionality between the distance of translation along x-axis and angle of rotation around x-axis of screw motion in the following way: for $p < 1$ the cross-section area between the blades decreases in the flow direction, for $p = 1$ the cross-section area is constant and for $p > 1$ the cross-section area increases.

To ensure the stability of the geometrical construction, as well as sufficient shape variability of the resulting helicoidal surface, parameter p is limited to $p \in (0, 2]$.

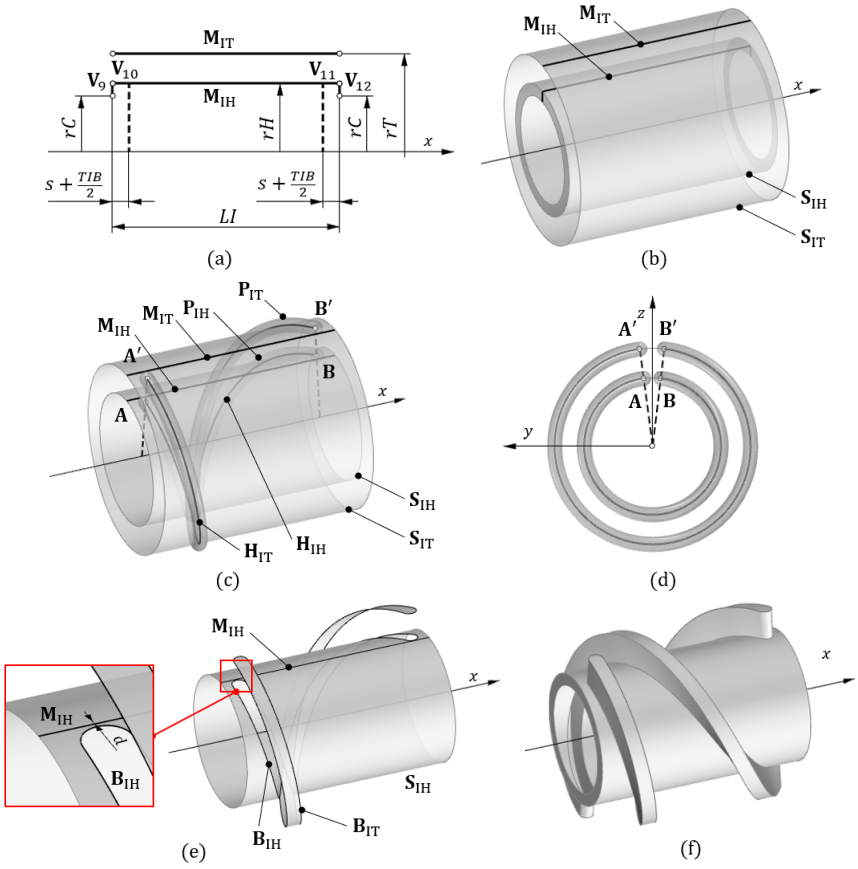

Fig. 4. Impeller modelling

Helix as a transcendental curve does not have a NURBS representation, therefore it cannot be modelled in a mathematically precise way in CAD systems. Helices $\mathbf{H}_{\mathrm{IH}}$ and $\mathbf{H}_{\mathrm{IT}}$ used in this design to define the impeller blade are constructed as 3rd-degree interpolation B-spline curves given by a set of definition points calculated on the theoretical helix (7) for $r = rH$ and $r = rT$. The number and distance of the theoretical points were chosen so that the deviations of the interpolation curves from the theoretical helices were less than the software tolerance 0.001 mm.

Helices $\mathbf{H}_{\mathrm{HI}}$ and $\mathbf{H}_{\mathrm{TI}}$ are used as directing curves for two pipes $\mathbf{P}_{\mathrm{IH}}$ and $\mathbf{P}_{\mathrm{IT}}$ with the same radius $TIB/2$ and rounded ends, see Fig. 4c and d. The boundary curves $\mathbf{B}_{\mathrm{IH}}$ and $\mathbf{B}_{\mathrm{TH}}$ are again obtained by intersection of the pipes with hub and tip cylindrical surfaces, i.e., $\mathbf{B}_{\mathrm{IH}} = \mathbf{S}_{\mathrm{IH}} \cap \mathbf{P}_{\mathrm{IH}}$ and $\mathbf{B}_{\mathrm{IT}} = \mathbf{S}_{\mathrm{IT}} \cap \mathbf{P}_{\mathrm{IT}}$, see Fig. 4e.

Pipe $\mathbf{P}_{\mathrm{IH}}$ is n_I times copied around x-axis to obtain cutting objects to create holes shaped according to curve $\mathbf{B}_{\mathrm{IH}}$ in the impeller hub.

To ensure the stability of the generated geometry, it is necessary to avoid intersections of the pipes with the mathematical boundaries of surfaces $\mathbf{S}_{\mathrm{IH}}$ and $\mathbf{S}_{\mathrm{IT}}$ along their meridians. Thus, the wrap angle w is limited to $w \in (0°, 360°)$. Moreover, the start point $\mathbf{A}$ of helix $\mathbf{H}_{\mathrm{IH}}$, and consequently, the start point $\mathbf{A}'$ of helix $\mathbf{H}_{\mathrm{IT}}$, are rotated around x-axis by angle corresponding to the safety distance d (set to 10% of the blade thickness TIB) between the boundary $\mathbf{B}_{\mathrm{IH}}$ and meridian $\mathbf{M}_{\mathrm{IH}}$, see Fig. 4d and the detail in Fig. 4e. Similarly, depending on the given wrap angle w, the constructive algorithm checks for unwanted intersection of pipe $\mathbf{P}_{\mathrm{IH}}$ and meridian $\mathbf{M}_{\mathrm{IH}}$ at the end of helix $\mathbf{H}_{\mathrm{IH}}$, and if so, the end points $\mathbf{B}$ and $\mathbf{B}'$ of both helices are rotated accordingly.

The impeller blade is constructed as a ruled surface given by boundaries $\mathbf{B}_{\mathrm{IH}}$ and $\mathbf{B}_{\mathrm{IT}}$ and the tip surface given by the inner part of tip cylindrical surface $\mathbf{S}_{\mathrm{IT}}$ after cutting by the pipe $\mathbf{P}_{\mathrm{IT}}$, see Fig. 4e. Finally, the impeller blade is copied n_I times around x-axis and the BRep of the impeller is finished, see Fig. 4f.

The above described procedure of impeller blades construction ensures all the required and easily parametrised geometrical properties of the impeller flow channels.

2.4. Diffuser modelling

Construction of the diffuser is derived from the position of point $\mathbf{V}_9$ given by (6). The construction is similar to the procedure used in the case of the straightener modelling, so its description is brief. The diffuser hub consists of two surfaces of revolution $\mathbf{S}_{\mathrm{DH}}$ and $\mathbf{S}_{\mathrm{D}}$ with meridians $\mathbf{M}_{\mathrm{DH}}$ and $\mathbf{M}_{\mathrm{D}}$, see Fig. 5a and b.

Meridian $\mathbf{M}_{\mathrm{DH}}$ is the piecewise linear curve with vertices

$$\mathbf{V}_{13} = (x_9 + LC, 0, rC), \mathbf{V}_{14} = (x_{13}, 0, rH), \mathbf{V}_{15} = (x_{13} + LBD + 2s). \tag{8}$$

Meridian $\mathbf{M}_{\mathrm{D}}$ is the 3rd-degree Bézier curve given by control points

$$\mathbf{V}_{15}, \mathbf{V}_{16} = (x_{15} + b_1, 0, rH), \mathbf{V}_{17} = (x_{13} + LD - b_2, 0, b_3), \mathbf{V}_{18} = (x_{13} + LD, 0, 0). \tag{9}$$

The mean camber line $\mathbf{C}_{\mathrm{D}}$ of the diffuser blade is the 3rd-degree Bézier curve given by control points

$$\mathbf{V}_{19} = (x_{13} + s + \tfrac{TDB}{2}, 0, -WDB + TDB), \mathbf{V}_{20} = (x_{19} + c_1, 0, 0),$$
$$\mathbf{V}_{21} = (x_{19} + LDB - TDB - c_2), \mathbf{V}_{22} = (x_{21} + c_2, 0, 0), \tag{10}$$

see Fig. 5a. The auxiliary surface $\mathbf{E}_{\mathrm{D}}$ is created by extrusion of mean camber line $\mathbf{C}_{\mathrm{D}}$ by vector $(0, -r-2)$. Pipes $\mathbf{P}_{\mathrm{DH}}$ and $\mathbf{P}_{\mathrm{DT}}$ have directing curves $\mathbf{C}_{\mathrm{DH}} = \mathbf{E}_{\mathrm{D}} \cap \mathbf{S}_{\mathrm{DH}}$ and $\mathbf{C}_{\mathrm{DT}} = \mathbf{E}_{\mathrm{D}} \cap \mathbf{S}_{\mathrm{DT}}$, see Fig. 5b. The meridian $\mathbf{M}_{\mathrm{DT}}$ of the cylindrical surface $\mathbf{S}_{\mathrm{DT}}$ is obtained by shifting the line segment $\mathbf{V}_{14}\mathbf{V}_{15}$ by vector $(0, 0, r - rH)$, therefore,

no gap is between the shroud and the diffuser blades. Boundary curves $\mathbf{B}_{DH}$ and $\mathbf{B}_{DT}$ of the diffuser blade are constructed as intersections of the extrusion and the pipes, i.e. $\mathbf{B}_{DH} = \mathbf{S}_{DH} \cap \mathbf{P}_{DH}$ and $\mathbf{B}_{DT} = \mathbf{S}_{DT} \cap \mathbf{P}_{DT}$, see Fig. 5c.

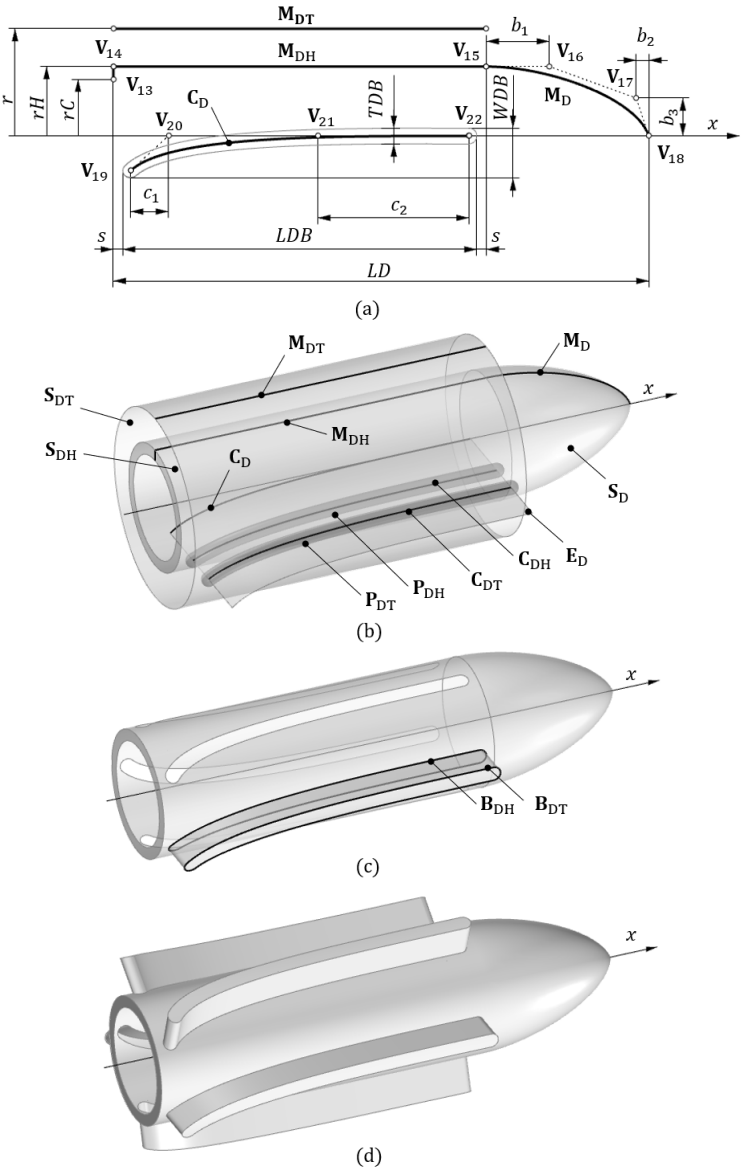

Fig. 5. Diffuser modelling

Pipe $\mathbf{P}_{\mathrm{DH}}$ is n_D times copied around x-axis to obtain cutting objects to create holes shaped according to curve $\mathbf{P}_{\mathrm{DH}}$ in the diffuser hub, see Fig. 5c. The diffuser blade is constructed as a ruled surface given by boundaries $\mathbf{B}_{\mathrm{DH}}$ and $\mathbf{B}_{\mathrm{DT}}$ and the tip surface given by the inner part of tip cylindrical surface $\mathbf{S}_{\mathrm{DT}}$ after cutting by the pipe $\mathbf{P}_{\mathrm{DT}}$, see Fig. 5c. Finally, the diffuser blade is copied n_D times around x-axis and the BRep of the diffuser is finished, see Fig. 5d.

2.5. Clutches modelling

Two clutches, see Fig. 2, are constructed as cylindrical surfaces of revolution $\mathbf{S}_{\mathrm{CL}}$ and $\mathbf{S}_{\mathrm{CR}}$ with linear meridians $\mathbf{M}_{\mathrm{CL}}$ and $\mathbf{M}_{\mathrm{CR}}$ given by endpoints $\mathbf{V}_5\mathbf{V}_9$ and $\mathbf{V}_{12}\mathbf{V}_{13}$, see Fig. 6. The coordinates of these points are given in (4), (6), (8) and (9). In the case the radius rC of the clutches is equal to the hub radius rH, the hub meridians $\mathbf{M}_{\mathrm{SH}}$, $\mathbf{M}_{\mathrm{IH}}$ and $\mathbf{M}_{\mathrm{DH}}$, see Figs. 3a, 4a and 5a, are not piecewise linear, but are given only by segments $\mathbf{V}_3\mathbf{V}_4$, $\mathbf{V}_{10}\mathbf{V}_{11}$ and $\mathbf{V}_{14}\mathbf{V}_{15}$ in the given order.

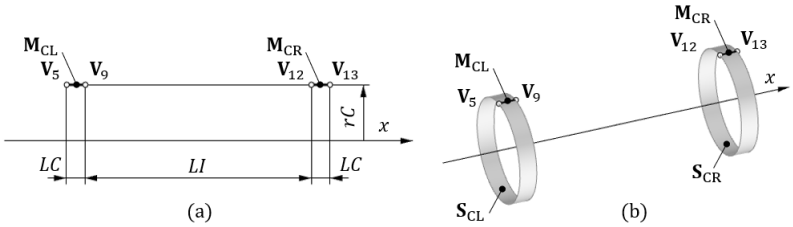

Fig. 6. Clutches modelling

2.6. Shroud, inlet, outlet and interfaces modelling

The shroud is a cylindrical surface of revolution consisting of three parts, see Fig. 7: $\mathbf{S}_{\mathrm{SS}}$, $\mathbf{S}_{\mathrm{SI}}$ and $\mathbf{S}_{\mathrm{SD}}$ with meridians $\mathbf{M}_{\mathrm{SS}} = \mathbf{V}_{23}\mathbf{V}_{24}$, $\mathbf{M}_{\mathrm{SI}} = \mathbf{V}_{24}\mathbf{V}_{25}$ and $\mathbf{M}_{\mathrm{SD}} = \mathbf{V}_{25}\mathbf{V}_{26}$, where

$$\mathbf{V}_{23} = (x_9 - LS, 0, r), \mathbf{V}_{24} = (x_{10}, 0, r),$$
$$\mathbf{V}_{25} = (x_{11}, 0, r), \mathbf{V}_{26} = (x_{23} + L, 0, r).$$

The shroud is closed by fictitious inlet $\mathbf{S}_{\mathrm{I}}$, a disk given by the left boundary $\mathbf{B}_{\mathrm{I}}$ of surface $\mathbf{S}_{\mathrm{SS}}$, and outlet $\mathbf{S}_{\mathrm{O}}$, a disk given by the right boundary $\mathbf{B}_{\mathrm{O}}$ of surface $\mathbf{S}_{\mathrm{SD}}$, see Fig. 7b.

Fictitious left $\mathbf{S}_{\mathrm{L}}$ and right $\mathbf{S}_{\mathrm{L}}$ interfaces are generated by revolution of meridians $\mathbf{M}_{\mathrm{L}} = \mathbf{V}_{10}\mathbf{V}_{24}$ and $\mathbf{M}_{\mathrm{R}} = \mathbf{V}_{11}\mathbf{V}_{25}$ around x-axis.

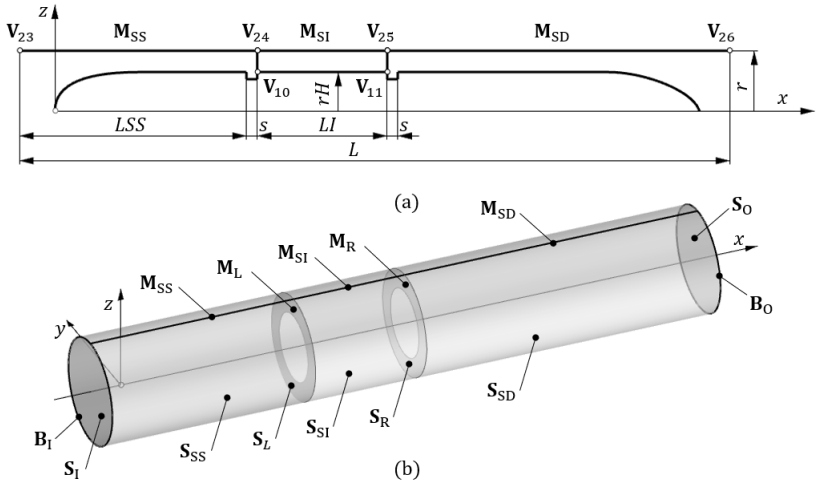

Fig. 7. Shroud, inlet, outlet and interfaces modelling

3. Triangular mesh generation and export to STL

The process of node-to-node triangular mesh generation consists of the following steps.

1. Blood pump mesh – To create a closed BRep of the axial blood pump, the functional surfaces of the straightener, impeller, diffuser and clutches visualised in Figs. 3h, 4f, 5d and 6b are joined into one closed polysurface. Since the construction procedures described above ensure the water-tightness of the resulting BRep, the tools for converting BRep to a triangular node-to-node mesh implemented in Grasshopper can be used. The obtained mesh, see Fig. 8, needs to be decomposed into meshes of individual surfaces and grouped into logical sets corresponding to the CFD computational blocks. Finally, the sets of meshes are exported as STL files into the output folder given in the set of input parameters listed in Table 1.
2. Shroud mesh – The closed BRep of the shroud is obtained by joining the cylindrical surfaces, inlet and outlet, see Fig. 7b. Then, the node-to-node triangular mesh is generated, decomposed and exported as STL files.
3. Interfaces meshes – The interfaces $\mathbf{S}_\mathrm{L}$ and $\mathbf{S}_\mathrm{R}$ do not belong to the closed BRep of either the blood pump or the shroud, therefore, conversion to a mesh cannot ensure coincidence of the vertices with the already generated meshes. The meshes of both interfaces were therefore not generated from surfaces $\mathbf{S}_\mathrm{L}$ and $\mathbf{S}_\mathrm{R}$, but created directly between the polygonal boundaries of the impeller and shroud meshes. The polygonal boundaries are located in planes $x = x_{10}$ and $x = x_{11}$, see Fig. 7a.

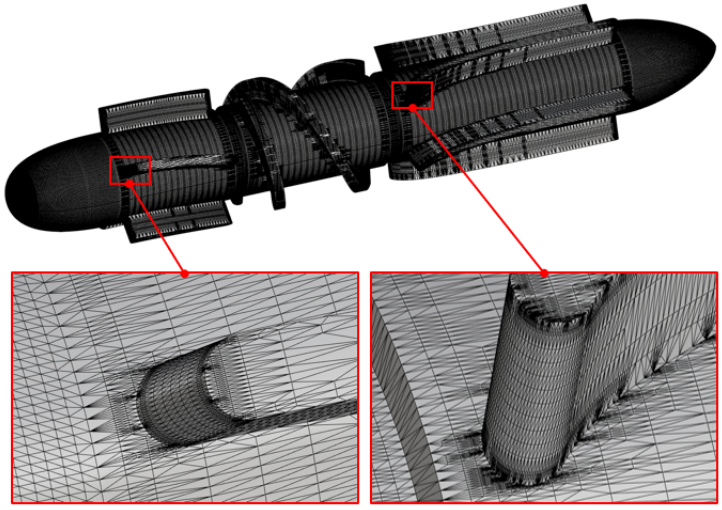

Fig. 8. Node-to-node triangular mesh of axial blood pump

4. CFD simulations

The simulations presented in this section of the paper should demonstrate the viability of the newly designed parametric CAD model of an axial blood pump in a fully automated advanced simulation workflow. The particular software tools being used and described here together with few selected examples of possible outputs of the performed simulations only aim to prove the declared quality and functionality of the newly proposed model set-up for research and development of VADs. The focus of this part of the paper is more on the computational test case and the associated workflow, rather than on detailed simulations and their results for certain particular VAD design.

The hydraulic performance and efficiency of the newly designed blood pump model is evaluated by the means of the CFD. There exist a number of readily available commercial software packages as well as open-source and in-house built codes that can be used for this purpose. The below described software package user case should thus be understood as one of the many possible choices for this task.

In the case presented, the advanced engineering software environment TCAE, developed by CFD SUPPORT LTD (www.cfdsupport.com), was used. This software is structured as a system of independent modules – TMESH, TCFD, TFEA, TOPT, and TCAA – which can function either as standalone tools or within a fully automated workflow. In this project, the following modules were utilized:

TMESH for creation of computational meshes,

TCFD for setting up the CFD calculation,

TOPT for setting up the optimisation and parametric calculations.

A significant advantage of TCAE lies in utilising various open-source third-party software packages and libraries as its computational core, most notably the OpenFOAM, CalculiX, netgen, gmsh and others. These modules can also easily be combined with additional third-party or in-house codes, enabling a high degree of customisation and extensions.

The graphical user interface of TCAE is built upon the open-source visualisation software ParaView, utilizing a modified version of its original GUI while preserving the majority of its core functionalities. TCAE can be operated both as a user-friendly "black box" or as a highly configurable and sophisticated simulation pipeline, depending on the user's expertise and requirements.

Moreover, the TCAE environment is capable of automatically generating comprehensive reports, both for individual CFD simulations and for optimisation tasks performed using the TOPT module. Additionally, a new software module, TBASE, is currently under development. This module will aim to build a structured database of simulation results for various test cases, serving as a foundation for generating fast and reliable surrogate models using machine learning and artificial intelligence (ML/AI) techniques. This will significantly accelerate the design and optimisation processes by reducing the need for repeated simulations.

Due to these advantages, the TCAE software was employed in this work to efficiently build the computational case and automatically generate all necessary configuration files and execution scripts, significantly simplifying the setup, execution, post-processing, and optimisation procedures. Nevertheless, since the computational core is based on open-source tools, users are not limited to the TCAE software and can independently build, configure, and manage the entire simulation workflow outside of TCAE if preferred.

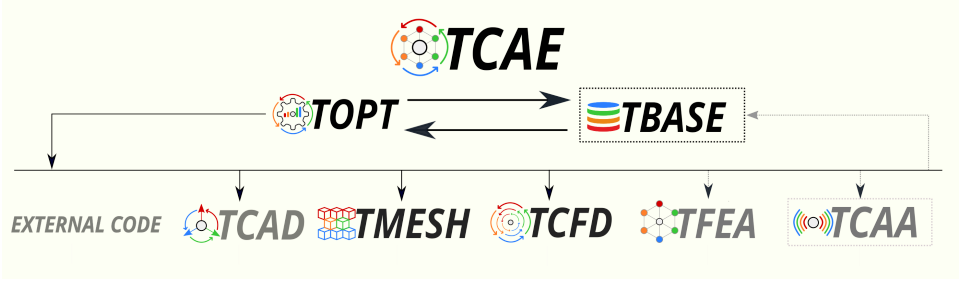

Fig. 9. System of independent modules

The aim of the performed and hereafter presented fluid flow simulations in the newly designed blood pump was to test the basic geometrical model, set-up the computational mesh generator and the flow solver. The focus is on the automated workflow, avoiding any later human intervention in the process, aiming for the CFD based shape optimisation as the final goal.

4.1. Computational grid generation

Based on the surface mesh of the model exported in the STL format by the Rhinoceros/Grasshopper software tools, the TMESH module within the TCAE is used to facilitate the generation of the computational grid by providing the necessary configuration and executing the freely available OpenFOAM [22] mesh generation utilities `blockMesh` and `snappyHexMesh`, which perform the actual grid generation. The resulting unstructured polyhedral (hexahedral-dominant) grid respects both the physical boundaries of the CAD model surface (the blood pump stator and rotor in this case) including the outer casing shroud, and the inlet/outlet artificial boundaries as well as the added interfaces between the static and rotating parts of the model. Special attention is paid to sufficient grid resolution close to solid boundaries, where the turbulent fluid flow solution can exhibit steep gradients. An example of such block-based grid generation using TMESH module within TCAE environment is shown in Fig. 10.

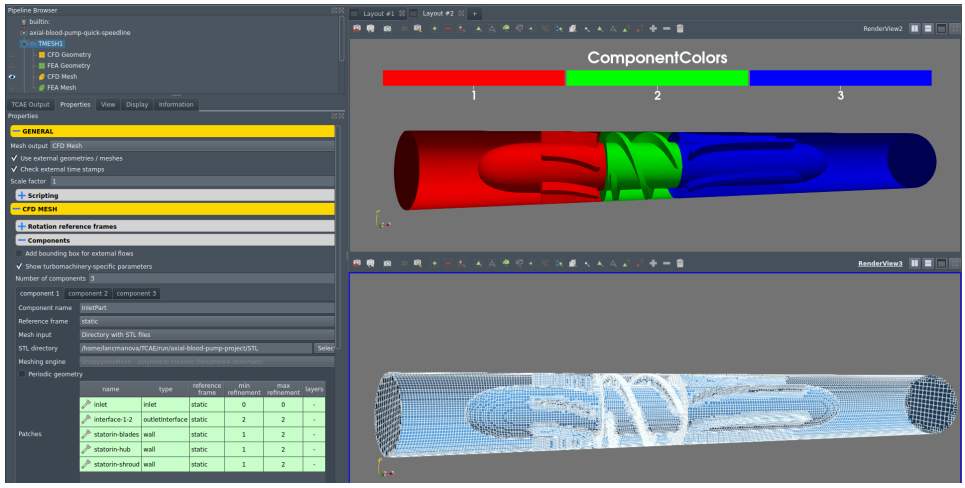

Fig. 10. The TMESH module environment with partially visible configuration settings for CFD mesh generation. The left panel shows a portion of the setup interface, including selected component definitions, mesh input, and patch refinement parameters. The top render window displays the geometry divided into components, colour-coded by region. The bottom window shows the resulting surface mesh generated by the SnappyHexMesh algorithm, with evident local refinement around geometrically complex areas of the axial blood pump

4.2. Flow simulations

The CFD simulations are performed by the open-source CFD toolbox OpenFOAM, which is set-up and called from the TCFD module of TCAE. For the computational purposes, the blood pump model is subdivided into two static and one rotating part. The static straightener and diffuser blocks are defined in a fixed reference frame, while a rotating frame of reference is considered for the impeller

block. This approach known as the Multiple Reference Frame (MRF) technique allows for simple and efficient approximation of flow problems with moving (often rotating) parts.

Instead of solving fully unsteady flow problem with moving and sliding boundaries, a steady flow simulation is performed with "frozen"-like rotor and all the effects of rotation are included as extra volume forces acting on the fluid in the local reference frame. The resulting velocity field needs thus be interpreted as being relative to the given static/rotating reference frame.

In order to determine the working parameters and characteristics of the proposed VAD over the range of admissible (biomedically relevant) operating regimes, a series of simulations was performed. In this case, the impeller operates at a constant speed of –8000 RPM, rotating around the body's axis (specifically, the x-axis). The negative sign indicates the direction of rotation as defined by the right-hand rule with respect to the global axis orientation. This approach is quite common in developing rotating fluid machines (pumps, for example), because it allows for obtaining characteristic curves from which the optimal working regime can be deduced. The same simulation approach (with fixed rotor speed and variable flow rate) was used, for example, in another well known VAD study [5].

Basically any single operating regime or a predefined series of simulations, with systematically varying a single parameter, such as the flow rate, rotor speed, or a selected geometrical feature of the pump design can be conducted in the basic setup. It is important to note that this scenario represents a planned (pre-defined) parametric study rather than an automated optimisation process.

As a typical example of such situation, the simulations presented thereafter are conducted over a range of working flow rates, with the prescribed inlet flow rate varied across ten discrete points increasingly up to approximately 1 ℓ/min. This range was chosen with reference to physiological conditions, particularly the wide variability observed in coronary blood flow (approximately 70–80 mℓ/min per 100 g of tissue at rest to up to 300–400 mℓ/min per 100 g during exertion [11]). Beyond this baseline flow rate range, additional simulations were performed at elevated flow rates to better reflect the typical operational range of blood pumps.

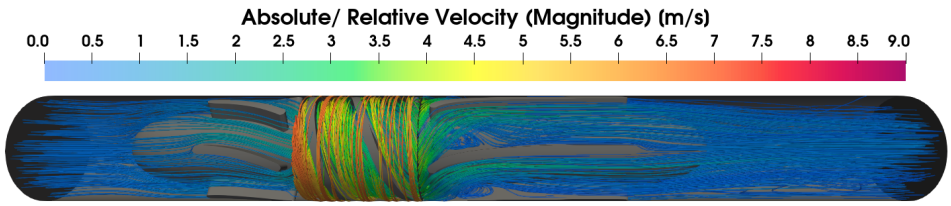

Fig. 11. Streamline visualisation of the flow field in rotating and stationary segments. In stationary segments, streamlines are computed based on the absolute velocity, while in rotating segments, the relative velocity (with respect to the rotating blades) is used. The colour scale indicates the velocity magnitude, using absolute and relative velocity depending on the segment. This visualisation serves as an illustrative example of the post-processing capabilities

For the purpose of this automated design study, the CFD solver was only tested for the flow of water (instead of blood), modelled as an incompressible Newtonian fluid. The flow was driven by a prescribed volumetric flow rate at the inlet, while fixed pressure was kept at the outlet. Turbulent flow was considered for the chosen working regime and the corresponding Reynolds number. The mathematical model is based on the (incompressible) Reynolds-Averaged Navier-Stokes (RANS) equations complemented by a two equation turbulence model. Specifically, the standard Shear Stress Transport (SST) $k-\omega$ turbulence model was chosen for the simulations presented hereafter. This model involves solving additional transport equations for the turbulent kinetic energy k and the specific rate of dissipation ω. Further details on the model formulation and its implementation can be found in [22–24].

The system of governing equations for the flow and turbulence quantities is discretised by a Finite-Volume Method (FVM). The convective (divergence) terms are treated within OpenFOAM using the `bounded Gauss limitedLinearV 1` scheme for the velocity field, while for the turbulence quantities (k, ω) the more robust (but less accurate) `bounded Gauss upwind scheme` was used. The gradients are approximated utilizing central difference (`linear` interpolation). The diffusion terms are discretized using the `Gauss linear corrected scheme`. A `linear` interpolation scheme is employed and the face normal gradient is computed using a `corrected` scheme. All these numerical approximation schemes are implemented and documented in the OpenFOAM [22].

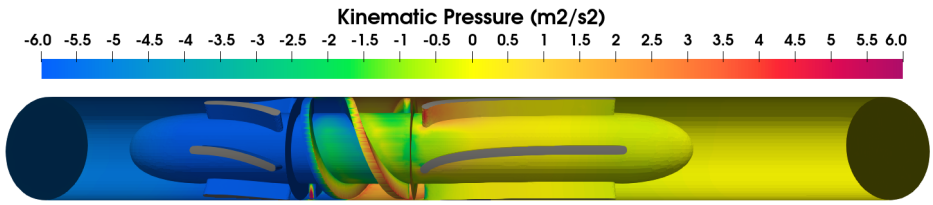

Fig. 12. Kinematic pressure for one flow regime, shown as a representative graphical output

4.3. CFD post-processing and data evaluation

The main focus of the whole paper is on presenting a new computational test case for VAD design and evaluation. The results shown and described (without deeper discussion or analysis) serve just as an example of outputs that can be obtained from the performed simulations, using the adopted software tools. Following the previously described CFD simulations, a sequence of datasets containing the 3D flow fields (including the local velocity, pressure and the turbulence quantities) were obtained for a range of working flow rates. Based on these datasets, the internal flow behaviour was evaluated using both qualitative and quantitative approaches. The qualitative evaluation focused on the visualisation of flow structures

such as vortices, regions of flow separation, and recirculation zones. The quantitative evaluation included the extraction of some bulk/integral quantities required to assess the blood pump performance under each of the considered flow regimes. These metrics include, but are not limited to, total pressure difference (outlet-inlet), torque, power, axial force and overall pump efficiency. Besides of these essential performance data characterising the particular design (shape) of the tested blood pump, some other auxiliary data are provided by the numerical CFD solver to assure and document the convergence and reliability of the numerical simulations.

The subsequent Figs. 13 – 15 present the key quantities obtained from the individual datasets corresponding to flow cases. These graphs serve as an illustration of the range of information that can be extracted from the CFD simulations and how such data can support assessment of a specific blood pump design performance.

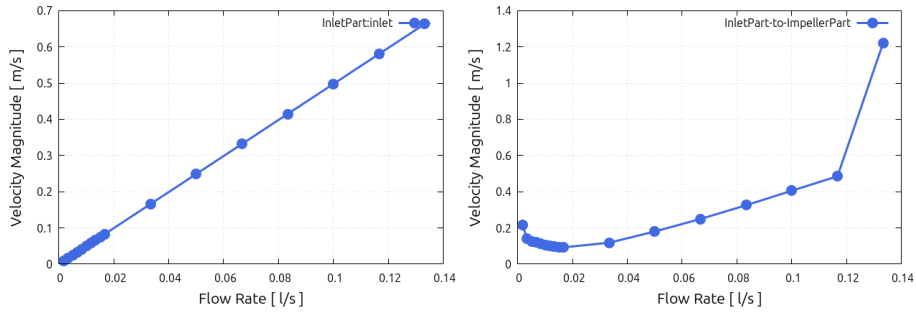

(a) Inlet (b) Impeller interface

Fig. 13. Velocity magnitude at different flow rates, representing the scalar value of fluid speed calculated as the square root of the sum of the squares of its velocity components

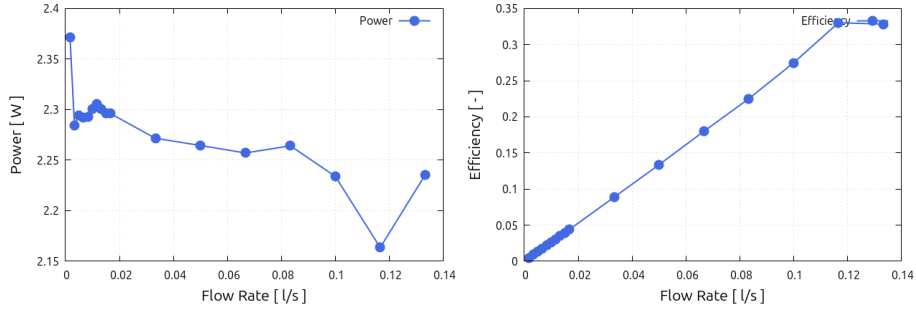

(a) Power (b) Efficiency

Fig. 14. Power and efficiency at different flow rates. The power is computed as the scalar product of the resulting torque and the angular velocity. Efficiency is calculated as the ratio of the product of total pressure difference and flow rate to the computed power

Furthermore, a detailed overview of the test case (such as mesh size, physical and turbulence models, fluid properties, numerical schemes, and simulation resource usage), along with the full set of analysed results, is summarised in an automatically generated report that presents the relevant data in the form of tables

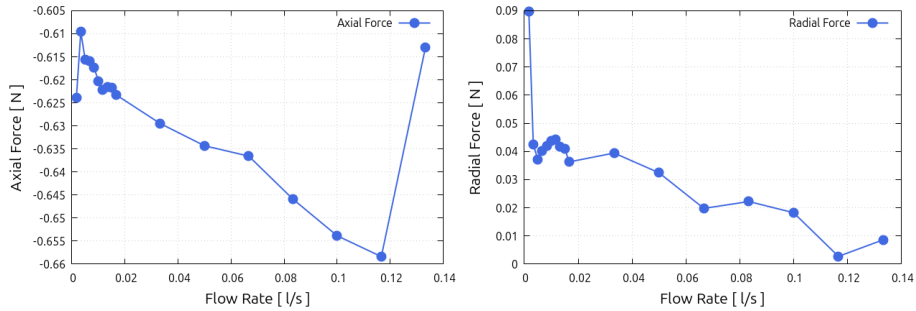

(a) Axial force (b) Radial force

Fig. 15. Axial and radial forces at different flow rates computed from the integrated pressure and viscous forces over the torque patch. Axial force is the projection onto the rotation axis, while radial force represents the orthogonal component

and graphs. The report primarily focuses on the evaluation of the performance and internal flow characteristics, rather than providing exhaustive details of the test case and computational setup. It is exported as a web-based document and made available to the customer or researcher for whom the blood pump design analysis was intended.

5. Automated shape optimisation

Another example of the use of the newly proposed VAD test geometry is the possible automated shape optimisation, where the fully parametric CAD model is essential. In the previous section, it was noted that simulations can be performed under a single operating regime or as a predefined series, systematically varying a single parameter such as flow rate, rotor speed, or a geometrical feature of the pump. However, the presented CAD-CFD model and workflow was already designed with shape optimisation in mind. All working blocks, the CAD geometry creation by Rhinoceros/Grasshopper, the grid generation and CFD simulations followed by automatic data postprocessing, evaluation and assessment within TCAE, can be linked into a unified workflow process. This is illustrated schematically in Fig. 16, which outlines the main options. The CFD simulations can be executed in a loop, with CAD geometry automatically adjusted based on the CFD outcomes and guided by an optimisation objective defined via a suitable cost function. The parametric nature of the CAD model is crucial here, as it allows a wide range of shape configurations to be explored in the search for optimal design.

Within the TCAE environment the optimisation tasks are carried out with the help of the TOPT module, which offers two main modes to chose from: Design of Experiments (DOE) or Optimisation.

In the DOE phase, parameter values can be defined as explicit lists or as linear or geometrical sequences. A Cartesian product of these sets forms a grid of points, where one simulation (computational case) is run for each point.

In contrast, the Optimisation mode in TOPT aims to identify parameter combinations that minimise or maximise a defined objective function. Two built-in algorithms are available: Golden Section Search and DIRECT (algorithm based on DIRECTv2 – DIvision of RECTangles, version 2). In both cases, TOPT first performs the DOE runs, identifies the best-performing design, and narrows the optimisation domain to its neighbouring DOE points (the DIRECT algorithm does not require a DOE initialisation. The number of initial samples can be set to zero).

It should be noted that optimisation in TOPT module is not limited to the built-in algorithms. External tools such as the Dakota [25] optimisation tool package can also be integrated, allowing for more advanced or customised optimisation strategies.

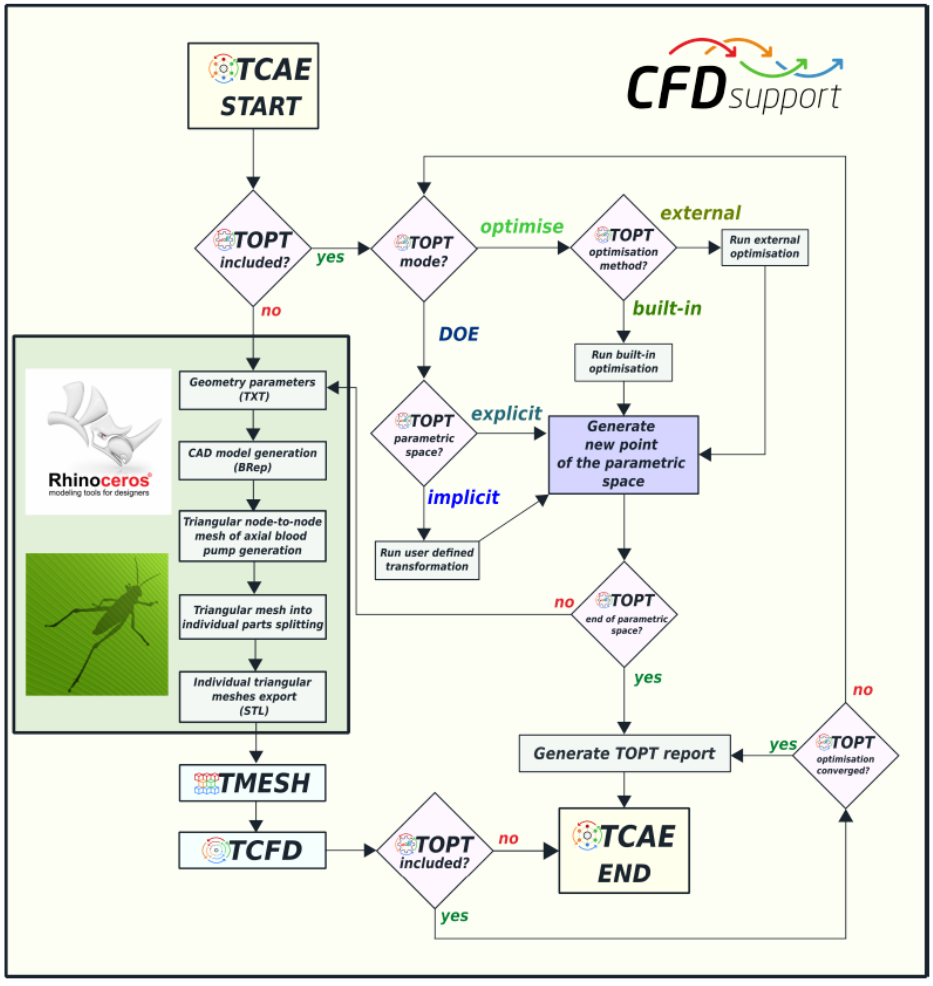

Fig. 16. Axial blood pump – automated process of 3D geometry generation, CFD simulation and optimisation in TCAE software

5.1. Optimisation evaluation and reporting

Within this section, an example of optimisation report including individual outputs is presented. It is an illustration of the successful integration of the newly developed parametric VAD model into an automated design process.

In addition to evaluating individual CFD cases, the adopted software workflow is fully equipped to handle parametric studies and optimisation tasks. All relevant input settings and simulation outputs are automatically collected to support systematic analysis and comparison across multiple design variants.

A key feature of this setup is the automatic generation of comprehensive, web-based reports, which combine tabulated data with a variety of visualisations that help to illustrate and evaluate the key performance metrics throughout the optimisation process.

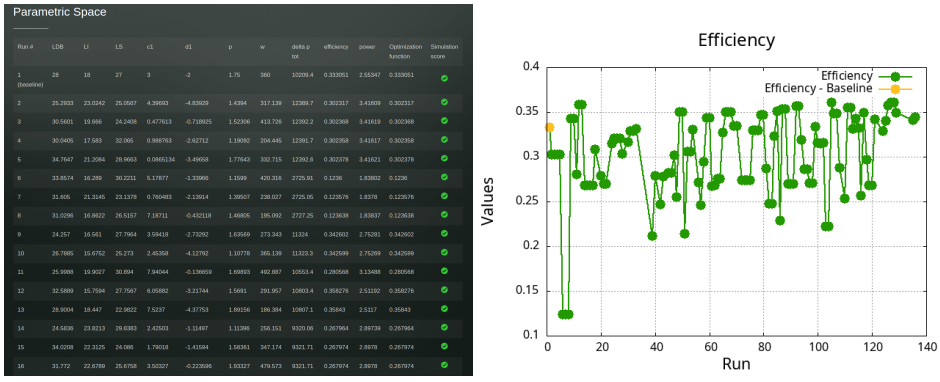

Fig. 17. A portion of an automatically generated HTML report from an optimisation run

Fig. 17 illustrates just a small portion of such report. The left side of the figure presents a partial output from the Parametric Space, listing a selection of simulation runs along with their corresponding input parameters and output values. Each row represents a single run (Run #), defined by unique set of input parameters (in this report: LDB, LI, LS, c_1, d_1, p, w) and followed by several output metrics. In addition to the tabulated values, the report includes plots showing the objective function, such as efficiency, throughout the sequence of simulations (see right side of the figure).

Further visualisations include diagrams such as "objective function vs. parameter" or "tracked quantity vs. parameter", providing further insight into the influence of individual parameters, see Fig. 18. The report enables straightforward comparison between different design configurations and highlights the best-performing cases. It offers an accessible way to trace how performance responds to changes in specific parameters. Some additional results and details regarding this initial optimisation series of simulations can be found in the Appendix of this paper.

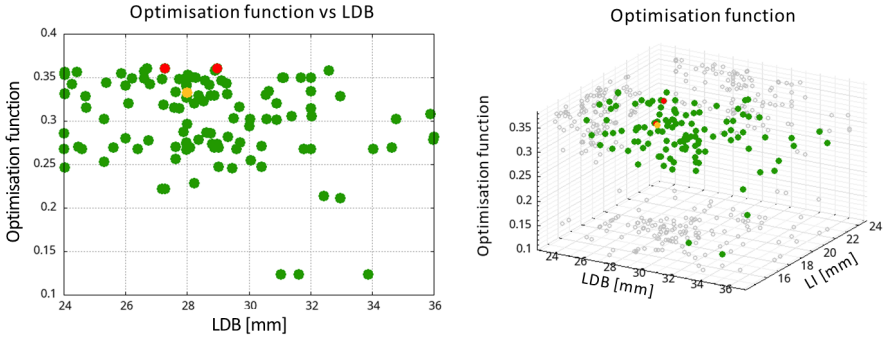

Fig. 18. An illustrative example of "objective function vs. parameter" and "tracked quantity vs. parameter" diagrams (LDB – Diffuser blades length, LI – Impeller length)

6. Conclusions and remarks

Within the present paper, a new fully parametric CAD model of a simple VAD was developed and successfully tested by integration into an advanced simulation workflow. The presented showcase of blood pump automated design, CFD evaluation and optimisation has proved the usability of the chosen workflow, adopted software tools and their mutual integration. Although all major components of the presented workflow, except for the Rhinoceros-based CAD module, are built on open-source codes and may be used independently, the TCAE environment offers a well-integrated and ready to use software for simulation, optimisation, and results evaluation. It allows users to benefit from a fully automated process while still providing full access to individual customisation if needed. The ongoing development of additional modules, such as the TBASE, further reinforces the software long-term potential, particularly in advanced design tasks such as geometry optimisation, evaluation of blood damage, or other performance related analyses.

The successfully tested geometrical design and full simulation setup (including computational grids and configuration files for OpenFOAM) will be made available to the research community for further development and testing. Together with more detailed reference simulation results and updated mathematical model setup, the whole newly developed test case will be made publicly available via the ERCOFTAC Knowledge Base Wiki page, where number of other test and benchmark cases are offered for research and development purposes. Thanks to the openly disclosed VAD geometry and the use of mainly open-source software tools, the future extensions and development of the associated mathematical models, numerical methods, and solution algorithms can be shared by the scientific community.

Our own aim and goal for future work regarding the presented VAD test case is to develop, implement and test further more advanced mathematical models including biomedical features such as the blood rheology, hemolysis and thrombosis in order to include these physiological processes in the automated shape optimisation process briefly introduced in this paper.

Appendix

This section presents some additional results from an initial series of simulations that focus on computational exploration of the geometric parameter space. The following results are not intended to represent a completed optimisation study, but rather to demonstrate the capabilities of the proposed parametric geometry and numerical workflow. The goal was to test how the design parameters can be systematically varied, how the workflow can handle multiple design points, and how the representative results can be analysed.

A total of 137 runs were performed at flow rate $Q = 5$ ℓ/min with seven design parameters (LDB, LI, LS, c_1, d_1, p, and w) allowed to vary within a pre-defined range, see Table 2 for details.

Table 2. Overview of the optimisation test setup including parameter definitions

Symbol	Parameter	Range
LDB	Diffuser blades length	$[25, 30]$
LI	Impeller length	$[17, 20]$
LS	Straightener length	$[22, 29]$
c_1	Straightener blade centre line definition	$[0, 5]$
d_1	Straightener blade centre line definition	$[-2, -5]$
p	Helix shape parameter	$[1, 1.8]$
w	Helix wrap angle	$[270, 450]$

The series of simulations was initiated from a baseline variant of the geometry, starting from which the seven selected parameters were allowed to vary automatically based on the optimization algorithm. Although just a very limited number (137) of individual simulations was run, some geometries can already be picked up showing a visible improvement (increase) in efficiency with respect to the original baseline design geometry. The summary of the original baseline design parameters and two improved design variants (best performing from the limited simulation series) are summarised in Table 3.

Table 3. Optimisation results – the baseline case and the two best-performing modified designs

Run #	LDB	LI	LS	c_1	d_1	p	w	Δp_{tot}	Efficiency	Power
1 (baseline)	28	18	27	3	-2	1.75	360	10209.4	0.333051	2.55347
105	28.963	16.6111	25.8251	2.67215	-3.05556	1.66049	315.556	11130.6	0.360276	2.57446
127	27.284	19.463	29.1955	5.03155	-2.45885	1.37654	355.556	11079.2	0.360276	2.56333

The efficiency shown in Table 3 is calculated for each variant from the total pressure difference Δp_{tot} and the power P. The two best-performing variants have the number 105 and 127. The efficiency η was found to be the same for both of them, however, the corresponding pressure difference and power are different. The increase in efficiency with respect to the baseline case was computed as

$$\Delta\eta = \frac{\eta_{\text{run}} - \eta_{\text{baseline}}}{\eta_{\text{baseline}}} \cdot 100\,\%, \tag{11}$$

which leads to

$$\Delta\eta_{105} = \frac{0.360276 - 0.333051}{0.333051} \cdot 100\,\% \approx 8.2\,\%, \tag{12}$$

$$\Delta\eta_{127} = \frac{0.360276 - 0.333051}{0.333051} \cdot 100\,\% \approx 8.2\,\%. \tag{13}$$

Thus, both optimised (improved) designs reached an increase in efficiency of approximately 8.2 % compared to the baseline case. The increased efficiency in these cases was achieved by different geometry adjustments. The variant 105 uses more pronounced rotor impeller helix changes together with more curved straightener blades, while the variant 127 has longer straightener section, leaving the other parts similar to the baseline design. These individual geometry changes can be seen from both the Table 3 showing the corresponding parameters, and the actual geometrical configurations shown in Fig. 19 together with the resulting kinematic pressure field.

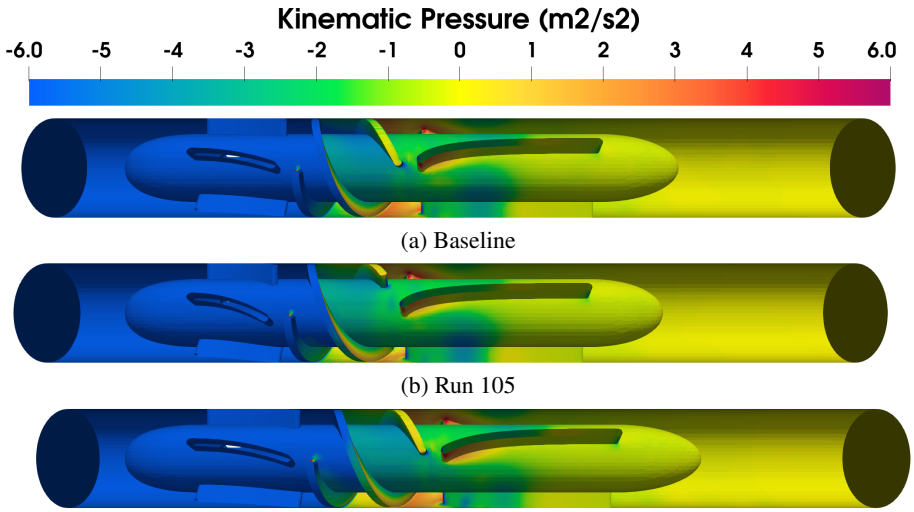

(a) Baseline

(b) Run 105

(c) Run 127

Fig. 19. Pressure distribution for the baseline and the two optimized (best performing) designs

The corresponding velocity field represented by streamlines coloured by velocity magnitude is shown in Fig. 20 for the three design variants. The flow fields are rather similar, with only minor visible changes in the wake behind the diffuser part, where the baseline design seems to generate more large-scale vortices in the wake compared to the two improved variants.

This first series of 137 exploratory simulations took in total about 15 hours of computational time on 10 cores. It provided a thorough test of the complete automatic design and simulation workflow, including an estimate of the corresponding

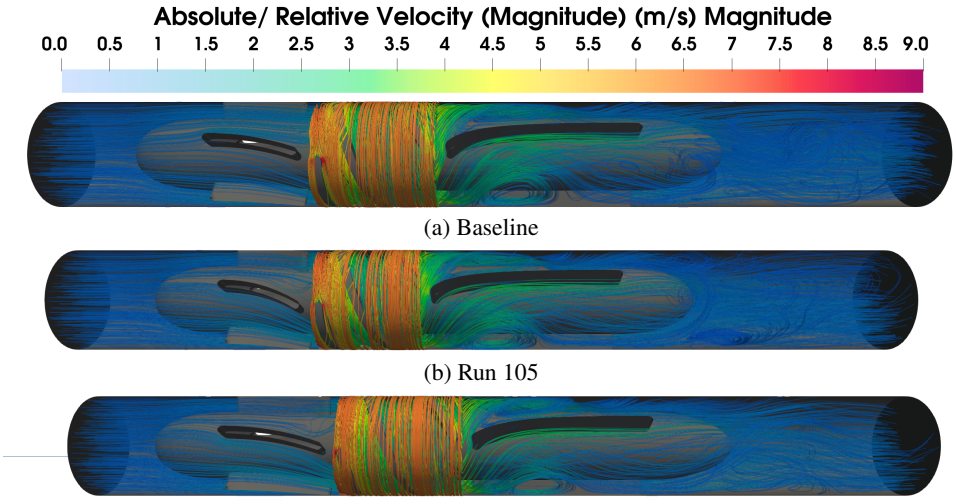

(a) Baseline

(b) Run 105

(c) Run 127

Fig. 20. Streamline visualisation of the flow field in rotating and stationary segments. In stationary segments, streamlines are computed based on the absolute velocity, while in rotating segments, the relative velocity (with respect to the rotating blades) is used. The colour scale indicates the velocity magnitude, using absolute and relative velocity depending on the segment

computational cost and required resources. In addition, it also brought some initial information about the relevance and relative importance of some of the geometrical parameters.

However, it should be emphasised that a complete and reliable optimisation study would require a detailed description and validation of the numerical simulation setup together with a much higher number of simulations being performed. Moreover, in the case of blood pumps, efficiency alone is not a sufficient criterion for the successful design selection. An appropriate cost function would need to incorporate multiple criteria, including, among others, the hemodynamic performance and hemocompatibility aspects.

Acknowledgements

The financial support for the present work was partly provided by the Czech Technical University in Prague, Faculty of Mechanical Engineering under the Grant SGS25/123/OHK2/3T/12, and partly by the Czech Academy of Sciences under the *Praemium Academiae of Š. Nečasová* and RVO:67985840.

The CFD parts of the research were conducted in the context of software development at CFD Support, s.r.o. (www.cfdsupport.com), with which two of the authors are affiliated. The authors gratefully acknowledge the company's technical environment and development activities that contributed to this work.

References

[1] K.H. Fraser, M.E. Taskin, B.P. Griffith, and Z.J. Wu. The use of computational fluid dynamics in the development of ventricular assist devices. *Medical Engineering & Physics*, 33(3):263–280, 2011. doi: 10.1016/j.medengphy.2010.10.014.

[2] B. Torner, L. Konnigk, N. Abroug, and H. Wurm. Turbulence and turbulent flow structures in a ventricular assist device – A numerical study using the large-eddy simulation. *International Journal of Numerical Methods in Biomedical Engineering*, 37(3):e3431, 2021. doi: 10.1002/cnm.3431.

[3] H. Yu, S. Engel, G. Janiga, and D. Thevenin. A review of hemolysis prediction models for computational fluid dynamics. *Artificial Organs*, 41(7):603–621, 2017. doi: 10.1111/aor.12871.

[4] L. Konnigk, B. Torner, M. Bruschewski S. Grundmann, and F.-H. Wurm. Equivalent scalar stress formulation taking into account non-resolved turbulent scales. *Cardiovascular Engineering and Technology*, 12(3):251–272, 2021. doi: 10.1007/s13239-021-00526-x.

[5] Flow in a ventricular assist device - pump performance & blood damage prediction: Application challenge AC7-03. https://www.kbwiki.ercoftac.org/w/index.php/AC7-03, 2022. Accessed: 2025-09-17.

[6] P.A. Smith, Y. Wang, S.A. Bieritz, L.C. Sampaio, W.E. Cohn, R.W. Metcalfe, and O.H. Frazier. Design method using statistical models for miniature left ventricular assist device hydraulics. *Annals of Biomedical Engineering*, 47(1):126–137, 2019. doi: 10.1007/s10439-018-02140-w.

[7] H.-M. Fan, F.-W. Hong, L.-D. Zhou, Y.-S. Chen, L. Ye, and Z.-M. Liu. Design of implantable axial-flow blood pump and numerical studies on its performance. *Journal of Hydrodynamics, Ser. B*, 21(4):445–452, 2009. doi: 10.1016/S1001-6058(08)60170-5.

[8] H.-M. Fan, F.-W. Hong, G.-P. Zhang, L. Ye, and Z.-M. Liu. Applications of CFD technique in the design and flow analysis of implantable axial flow blood pump. *Journal of Hydrodynamics, Ser. B*, 22(4):518–525, 2010. doi: 10.1016/S1001-6058(09)60084-6.

[9] V. Kannojiya, A.K. Das, and P.K. Das. Proposal of hemodynamically improved design of an axial flow blood pump for lvad. *Medical & Biological Engineering & Computing*, 58:401–418, 2020. doi: 10.1007/s11517-019-02097-5.

[10] D. Carswell, D. McBride, T.N. Croft, A.K. Slone, M. Cross, and G. Foster. A CFD model for the prediction of haemolysis in micro axial left ventricular assist devices. *Applied Mathematical Modelling*, 37(6):4199–4207, 2013. doi: 10.1016/j.apm.2012.09.020.

[11] J.-P. Barral and A. Croibier. Homeostasis of the cardiovascular system. In J.-P. Barral and A. Croibier, editors, *Visceral Vascular Manipulations*, pages 46–60. Churchill Livingstone, Oxford, 2011. doi: 10.1016/B978-0-7020-4351-2.00003-X.

[12] S. Lv, Z.-P. He, G.-M. Liu, and S.-S. Hu. Numerical simulation on the effect of impeller radial gap on hemodynamics and hemocompatibility of a centrifugal blood pump. *Computer Methods in Biomechanics and Biomedical Engineering*, pages 1–12, 2025. doi: 10.1080/10255842.2024.2448299.

[13] L. Wiegmann, S. Boës, D. de Zélicourt, B. Thamsen, M. Schmid Daners, M. Meboldt, and V. Kurtcuoglu. Blood pump design variations and their influence on hydraulic performance and indicators of hemocompatibility. *Annals of Biomedical Engineering*, 46(3):417–428, 2018. doi: 10.1007/s10439-017-1951-0.

[14] G. Bao, Y. Bazilevs, J.-H. Chung, P. Decuzzi, H.D. Espinosa, M. Ferrari, H. Gao, S.S. Hossain, T.J.R. Hughes, R.D. Kamm, W.-K. Liu, A. Marsden, and B. Schrefler. USNCTAM perspectives on mechanics in medicine. *Journal of The Royal Society Interface*, 11(97):20140301, 2014. doi: 10.1098/rsif.2014.0301.

[15] T. Bodnár, I. Linkeová, and L. Pirkl. Design and numerical simulation of an axial blood pump. In Bodnár T. Šimurda D., editor, *Proceedings Topical Problems of Fluid Mechanics 2025*, pages 23–30, Prague, 2025. Institute of Thermomechanics CAS. doi: 10.14311/TPFM.2025.004.

[16] Y. Zhang, S.S. Hu, J.-Y. Zhou, H.-S. Sun, H. Zhang, Z. Zheng, X.-D. Zhu, G.-R. Li, X.-M. Gui, Z. Zhan, and D.-H. Jin. Design and performance testing of an axial-flow ventricular assist device developed at the Fu Wai Hospital in Beijing. *The International Journal of Artificial Organs*, 31(11):983–987, 2008. doi: 10.1177/039139880803101108.

[17] A. Gouskov, F. Sorokin, E. Banin, A. Krupnin, and S. Skoryukov. Experimental validation of a numerical model of an axial circulatory assist blood pump. *Biomedical Engineering*, 53:77–81, 2019. doi: 10.1007/s10527-019-09881-5.

[18] L. Piegl and W. Tiller. *The NURBS Book*. Springer-Verlag, Berlin Heidelberg, 1997. doi: 10.1007/978-3-642-59223-2.

[19] V. Shapiro. Solid Modeling. In G. Farin, J. Hoschek, and M.-S. Kim, editors, *Handbook of Computer Aided Geometric Design*, chapter 20, pages 473–518. North-Holland, Amsterdam, 2002. doi: 10.1016/B978-044451104-1/50021-6.

[20] M.K. Agoston. Surfaces in computer graphics. In *Computer Graphics and Geometric Modeling: Implementation and Algorithms*, chapter 12, pages 472–536. Springer London, London, 2005. doi: 10.1007/1-84628-108-3_12.

[21] D. Salomon. *Curves and Surfaces for Computer Graphics*. Springer, New York, 2007. doi: 10.1007/0-387-28452-4.

[22] OpenCFD Ltd. OpenFOAM User Guide. online, 2003. https://www.openfoam.com/documentation/user-guide.

[23] F.R. Menter. Improved two-equation $k-\omega$ turbulence models for aerodynamic flows. Technical Memorandum NASA-TM-103975, NASA, 1992.

[24] F.R. Menter, M. Kuntz, R. Langtry, et al. Ten years of industrial experience with the sst turbulence model. *Turbulence, Heat and Mass Transfer*, 4(1):625–632, 2003.

[25] B.M. Adams, W.J. Bohnhoff, K.R. Dalbey, M.S. Ebeida, J.P. Eddy, M.S. Eldred, R.W. Hooper, P.D. Hough, K.T. Hu, J.D. Jakeman, M. Khalil, K.A. Maupin, J.A. Monschke, E.E. Prudencio, E.M. Ridgway, P. Robbe, A.A. Rushdi, D.T. Seidl, J.A. Stephens, L.P. Swiler, and J.G. Winokur. Dakota 6.21.0 documentation. technical report sand2024-15492o. Technical report, Sandia National Laboratories, Albuquerque, NM, 2024.